

# The Evolution of Substructure in Galaxy, Group and Cluster Haloes III: Comparison with Simulations

James E. Taylor<sup>1\*</sup>† and Arif Babul<sup>2</sup>

<sup>1</sup>*Denys Wilkinson Building, 1 Keble Road, Oxford OX1 3RH, United Kingdom*

<sup>2</sup>*Elliott Building, 3800 Finnerty Road, Victoria, BC, V8P 1A1, Canada*

23 July 2018

## ABSTRACT

In a previous paper, we described a new method for including detailed information about substructure in semi-analytic models of halo formation based on merger trees. In this paper, we compare the predictions of our model with results from self-consistent numerical simulations. We find that in general the two methods agree extremely well, particularly once numerical effects and selection effects in the choice of haloes are taken into account. As expected from the original analyses of the simulations, we see some evidence for artificial overmerging in the innermost regions of the simulated haloes, either because substructure is being disrupted artificially or because the group-finding algorithms used to identify substructure are not detecting all the bound clumps in the highest-density regions. Our analytic results suggest that greater mass and force resolution may be required before numerical overmerging becomes negligible in all current applications. We discuss the implications of this result for observational and experimental tests of halo substructure, such as the analysis of discrepant magnification ratios in strongly lensed systems, terrestrial experiments to detect dark matter particles directly, or indirect detection experiments searching for positrons, gamma-rays, neutrinos or other dark matter decay products.

**Key words:** gravitational lensing – methods: numerical – galaxies: clusters: general – galaxies: formation – galaxies: haloes – dark matter.

## 1 INTRODUCTION

There is now very strong evidence from observations of the microwave background (Spergel et al. 2003), galaxy redshift surveys (e.g. Tegmark et al. 2004), weak lensing measurements (e.g. Rhodes et al. 2004), and modelling of the Lyman- $\alpha$  forest (e.g. Kim et al. 2004), that most of the matter in the universe is non-baryonic dark matter, and that the power spectrum of density fluctuations in this component extends to subgalactic scales, as expected in ‘cold’ dark matter (CDM) models. The implications of the CDM power spectrum for structure formation are well established. Dark matter haloes, the dense regions that surround galaxies, groups and clusters, form from the bottom up, through the merging of progressively larger structures. This process of hierarchical merging has been studied extensively, and the overall properties of galaxy or cluster haloes formed in this way are now fairly well determined.

To learn more about dark matter, and to search for fea-

tures in the power spectrum that could reveal new phases in the evolution of the very early universe, we must push the theory of structure formation to smaller scales. Most of our current understanding of the properties of dark matter on subgalactic scales comes from numerical simulations of structure formation. These simulations have been used to determine the evolution of large-scale structure and the formation of CDM haloes on scales ranging from the current horizon (Kauffmann et al. 1999) down to the local neighbourhood (e.g. Mathis et al. 2002). Furthermore, by selectively re-simulating sections of a large volume at higher resolution, recent studies have been able to ‘zoom in’ on single objects, resolving the substructure within individual haloes in exquisite detail (e.g. recent work by De Lucia et al. 2004; Gill, Knebe, & Gibson 2004a; Gill et al. 2004b; Gao et al. 2004a, 2004b; Diemand et al. 2004c; Weller, Ostriker & Bode 2004; Reed et al. 2004)

There is a hard limit, however, to the dynamic range that can be achieved using this approach of selective re-simulation. Structure formation mixes information on many different scales as haloes form. To model the formation of a dark matter halo accurately, one needs to include the

\* PPARC Fellow

† email: jet@astro.ox.ac.uk

effects of very long-wavelength fluctuations as well as the smaller fluctuations that produce substructure. The minimum scale that can be included in any self-consistent simulation of the formation of a present-day halo is determined by the requirement that the largest fluctuations in the volume studied still be in the linear regime at the present day, and by the finite numerical resolution available computationally. For the highest-resolution simulations that are currently feasible, this leads to a minimum mass scale for resolved substructure of around  $10^{-4}$ – $10^{-5}$  of the mass of the main halo considered. To study halo substructure below this mass limit requires analytic or semi-analytic extensions to the numerical results. It is precisely this sort of small-scale information, however, that is required in many current applications including galaxy dynamics, strong lensing, direct or indirect dark matter detection, or tests of dark matter physics in general.

In earlier work (Taylor & Babul 2001, TB01 hereafter), we developed a model for dynamical evolution of satellites orbiting in the potential of larger system. This model includes simple treatments of dynamical friction, tidal mass loss and tidal disruption. It calculates satellite evolution over a many short timesteps, rather like a restricted  $N$ -body simulation, but uses only global properties of the satellite to determine its evolution, thus reducing the computational expense considerably. More recently (Taylor & Babul 2004a, paper I hereafter), we have applied this model of satellite evolution to the merging subcomponents involved in the hierarchical formation of galaxy, group or cluster haloes, creating a full semi-analytic model of halo formation. In a second paper (Taylor & Babul 2004b, paper II hereafter), we presented the basic predictions of this model, including distributions of subhalo mass, circular velocity, location and merger epoch, and the correlations between these properties. We found results similar to those of recent numerical studies, as well as for a few systematic differences.

In this paper, we compare the predictions of the semi-analytic model directly with the results of self-consistent numerical simulations of halo formation. This comparison is particularly interesting, since the only free parameters in the semi-analytic model were fixed in paper I, either by matching restricted simulations of individual subhaloes (to fix the parameters of the dynamical model), or by assuming self-similarity in the merging process (to fix the one free parameter in the pruning method). Thus we have no remaining parametric freedom when comparing our results to self-consistent simulations, making the comparison a meaningful one. Overall, we will show that there is reasonable agreement between the semi-analytic and numerical results, particularly in regions where both are expected to be accurate, but also that there are systematic differences between their predictions. These could reflect inaccuracies in the semi-analytic model, but closer examination of the numerical results suggests that at least part of the discrepancy is due to artificial numerical effects in the simulations. The quantitative estimate of the magnitude of these effects has interesting implications for the analysis of several recent observational results.

The outline of this paper is as follows. In section 2, we summarise briefly the semi-analytic model developed in paper I. In section 3, we describe the six simulated haloes used in our comparison, and analyse the general properties

of their subhalo populations. In section 4, we compare the properties of individual subhaloes, as well as the cumulative distributions of subhalo mass or circular velocity, in semi-analytic model and in the numerical simulations. In particular, we examine the evidence that the central regions of the simulated haloes are subject to artificial overmerging. In section 5, we consider the implications of overmerging in two particular areas, the modelling of strongly-lensed systems, and the analysis of direct detection experiments. We summarise our conclusions in section 6. Finally, we note that as in papers I and II, in this paper we will generally consider results for the former ‘standard’ CDM (SCDM) cosmology with  $h = 0.5$  and  $\sigma_8 = 0.7$ , because the simulations we compare to assumed this cosmology. In general, our main results depend only weakly on cosmology, as discussed in paper II.

## 2 REVIEW OF THE SEMI-ANALYTIC MODEL

In paper I, we introduced a semi-analytic model for studying the formation of dark matter haloes and the evolution of their substructure. In this section we will review briefly the main features of this model. The model is explained fully in TB01 and paper I, and a more detailed summary is given in paper II.

The semi-analytic model consists of several components: a method for generating merger trees, an algorithm for ‘pruning’ these trees, to determine how many distinct satellites merge into the main system within the tree, an analytic model to describe the subsequent evolution of these satellites, and a model for the concurrent evolution of the main system. The halo merger histories are generated using the merger-tree algorithm of Somerville and Kolatt (1999). Higher order branchings in these trees are then pruned, using the method described in paper I, to determine whether each branch merging with the main trunk contributes a single subhalo or a group of associated subhaloes to the main system. This produces a single list of subhaloes merging with the main system at various redshifts. Each subhalo from this final list is placed on a random orbit starting at the virial radius of the main system, and evolved using the analytic model of satellite dynamics described in TB01, experiencing orbital decay due to dynamical friction, and heating and stripping due to tidal forces. Haloes which were associated with a given parent before pruning fall in together with the parent on similar orbits, as part of a kinematic group.

The properties of the main system also change over time, its mass growing according to the merger tree and its concentration changing according to the relations in Eke, Navarro, & Steinmetz (2001, ENS01 hereafter). Although no baryonic component is included in the models presented here, one can easily be added, given a prescription for gas cooling and star formation. We assume, unless specified otherwise, that the main system has a Moore density profile and a concentration or scale radius given by the relations in ENS01. Our fiducial system, a  $1.6 \times 10^{12} M_\odot$  halo at  $z = 0$  in a SCDM cosmology, has a concentration  $c_M = 10.3$ , a scale radius  $r_{s,M} = 30.5$  kpc, a virial radius  $r_{\text{vir},m} = 314.1$  kpc, and a virial velocity (or circular velocity at the virial radius)  $v_{\text{vir},m} = 148 \text{ km s}^{-1}$ . We note that this concentration is typical for a galaxy of this mass (ENS01); galaxy clusters would be about half as concentrated, this difference should

be kept in mind when comparing our results with simulations of more massive systems. On the other hand, real galaxy haloes have large concentrations of baryonic material at their centres, and through adiabatic contraction they may have become more concentrated than the systems considered here; this possible difference should be kept in mind when comparing with observations.

In all, the dynamical model has two main free parameters – the Coulomb logarithm  $\Lambda_s$  which modulates dynamical friction, and the heating coefficient  $\epsilon_h$  which modulates mass loss. (A third parameter discussed in TB01, the disk logarithm  $\Lambda_d$ , is not used here since we are considering evolution in a single-component potential). The precise disruption criterion (say the fraction of the binding radius used to define  $f_{\text{dis}}$ ), the form chosen for the density profile of the satellites and the profile of the main system, and various other model choices will also affect some of our results, though not very strongly. We discuss the model-dependence of our results in paper II. Here we generally present results for the default parameter values discussed in paper I, specifically  $\Lambda_s = 2.4$  (where the magnitude of dynamical friction scales as  $\Lambda(M) = \Lambda_s + \ln(M_h/140 M_s)$  if  $m < M/140$ , and  $\Lambda(M) = \Lambda_s$  for  $m \geq M/140$ ), and  $\epsilon_h = 3.0$ . The disruption criterion assumes either  $f_{\text{dis}} = 0.5$  (model A) or  $f_{\text{dis}} = 0.1$  (model B). Given these parameter choices, the pruning parameters are fixed iteratively as discussed in paper I.

### 3 NUMERICAL PREDICTIONS FOR HALO SUBSTRUCTURE

#### 3.1 Review of the simulations

To test the accuracy of our model and compare it with fully numerical results, we will examine the properties of substructure in six different haloes extracted from high-resolution simulations. The basic properties of these haloes are listed in table 1, along with the references in which the original simulations are described. The subhalo lists extracted from these simulations were supplied by their respective authors; in some cases they differ slightly from the data sets used in the references listed, as the simulations have been reanalysed subsequently. We will start by examining these datasets in detail, to quantify how much scatter is expected in subhalo properties from one system to another. We note that a much larger sample of  $\Lambda$ CDM haloes, simulated at comparable or higher resolution, has recently become available (De Lucia et al. 2004; Desai et al. 2004; Gill et al. 2004a, 2004b; Diemand et al. 2004c; Gao et al. 2004a, 2004b; Weller et al. 2004; Reed et al. 2004). Wherever possible, we will also consider this more recent work.

The objects named ‘Coma’ and ‘Virgo I’ are a massive and an intermediate-mass cluster halo, respectively, extracted from the simulations of Moore et al. 1998 (M98 hereafter). ‘Virgo IIa’ and ‘Virgo IIb’ are actually two different outputs from the same simulation of a Virgo-sized cluster, at redshifts 0 and 0.1 respectively. The cluster, described in Ghigna et al. 2000 (G00), is a higher-resolution re-simulation of a system first discussed in Ghigna et al. 1998 (G98). ‘Andromeda’ and the ‘Milky Way’ (the ‘Local Group’) are a close pair of galaxy-size haloes selected because of their resemblance to the two main systems in the real Local Group.

They are described in Moore et al. 1999b (M99b) and their substructure is analysed in Moore et al. 1999a (M99a).

These simulations were all performed in a ‘standard’ CDM ( $\Omega = 1$ ,  $h = 0.5$ ,  $\sigma_8 = 0.7$ ) cosmology. For purposes of comparison, we have generated our semi-analytic results assuming the same cosmology. The simulations cover a wide range of mass, and also a range in mass resolution and softening length, as indicated in table 1. They typically have several million particles within the virial radius, and a softening length of less than 1 percent of the virial radius. Although these simulations were performed several years ago, this combination of mass and force resolution has only recently been surpassed more than a factor of 1.5–2, and even then only in a very few simulations (e.g. Diemand et al. 2004c; Gao et al. 2004b). Virgo IIa and IIb have particularly high force resolution, as well as their high mass resolution. Coma has comparable mass resolution but more softening, while Virgo I, Andromeda and the Milky Way have lower mass resolution, and are also more heavily softened.

The substructure in these simulations was identified using the group finder SKID (Stadel 2001; available at <http://hpcc.astro.washington.edu/tools>). SKID identifies groups by finding local maxima in the density field, linking them together with a friends-of-friends algorithm, and then removing unbound particles iteratively. It produces estimates of the structural properties of each bound group of particles, including its total mass, its outer radius (the radius of the outermost bound particle), the radius at which its rotation curve peaks, and the value of the peak circular velocity. We have all of this information for the subhaloes in the Virgo II and Local Group simulations, and more limited information for the first two simulations. Of the various properties measured by SKID, we will assume that the total mass  $M_s$  is slightly more reliable than the outer radius, since the latter depends on the position of the single outermost particle. We will also consider the peak velocity  $v_{p,s}$  of each subhalo, as an indicator of its density profile and concentration.

We note that the structural properties of individual subhaloes in simulations are subject to important numerical effects. This has been demonstrated by carrying out idealised simulations of satellites in fixed potentials, at much higher resolution than is possible in self-consistent simulations where haloes form naturally from cosmological initial conditions (Hayashi et al. 2003, H03 hereafter; Kazantzidis et al. 2004). Even in a static potential, determining rotation curves for subhaloes to an accuracy of 10 percent after a few orbits requires resolving them with more than  $5 \times 10^5$  particles initially (i.e. a few times  $10^4$  after mass loss – Kazantzidis et al. 2004). Given the steepness of the cumulative velocity function, a 10 percent error in velocity can change the number of subhaloes at a given velocity by 30–40 percent, so even errors of this order should be taken into account. Force softening also has a direct effect on small subhaloes, placing an upper limit on their circular velocity when they are sufficiently dense. Finally, the group-finding algorithms used to identify substructure in self-consistent simulations often depend explicitly on the local density of a subhalo’s environment. Thus subhalo properties should be treated with caution even in high-resolution simulations. We will discuss these issues further in sections 4.1 and 4.2 below.

Finally, we need to normalise the properties of each set of numerical subhaloes, in order to compare them on

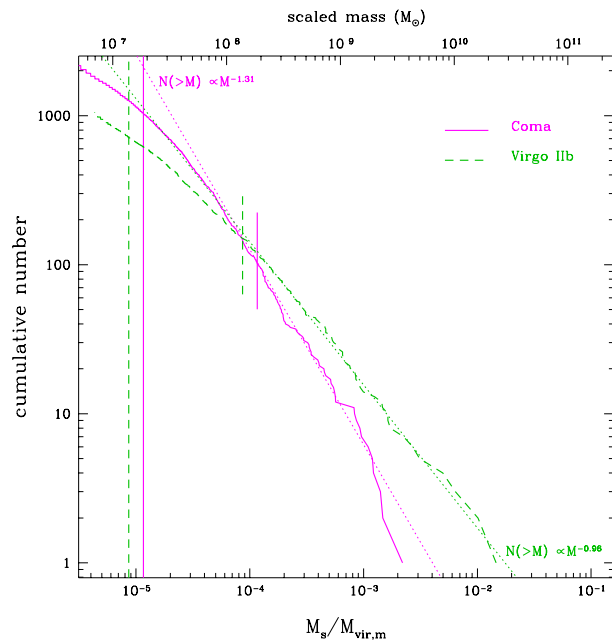


**Figure 1.** The cumulative relative mass functions for the two highest-resolution simulations, Coma (solid line) and Virgo II (dashed line; shown at  $z = 0.1$ ). The dotted lines are power-laws with slopes  $-1.31$  and  $-0.96$ . The top axis shows the equivalent subhalo mass in a system with the fiducial mass  $1.6 \times 10^{12} M_{\odot}$ . The vertical lines indicate the 32-particle and 320-particle mass-resolution limits for each simulation.

the same footing. To do so, we divide the mass of each subhalo by  $M_{\text{vir,m}}$ , the mass of its parent halo within its virial radius, and divide the peak velocity of the subhalo by  $v_{\text{vir,m}}$ , the circular velocity of its parent halo at the virial radius<sup>1</sup>. Where necessary we can then scale these relative values to our semi-analytic model values, multiplying them by  $M = 1.6 \times 10^{12} M_{\odot}$  and  $148 \text{ km s}^{-1}$ , respectively. When counting the number of subhaloes over some mass or velocity threshold, we generally limit ourselves to the region within the virial radius of the main halo, since the semi-analytic results are incomplete beyond the virial radius, as they do not include subhaloes that have not yet fallen in past this point. This procedure produces relative distributions or scaled distributions that can easily be compared with one-another and with the semi-analytic results. Furthermore, we expect the properties of each system to be similar when scaled in this way, since structure formation should be fairly close to scale-invariant over the range of halo masses considered here.

## 3.2 Scatter in the numerical distributions

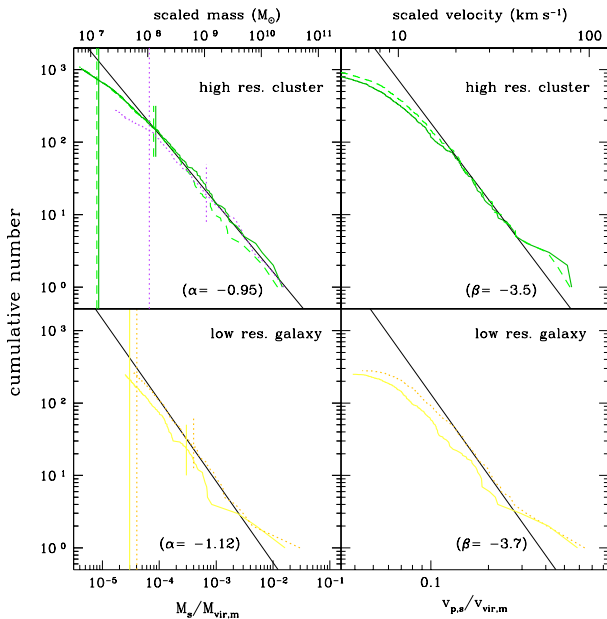
### 3.2.1 The shape of the mass function

Fig. 1 shows the cumulative relative mass functions for all subhaloes within the virial radius of two systems, Coma (solid line) and Virgo IIb (dashed line). The full vertical lines indicate the mass for each simulation corresponding to 32 particles. In the original analysis of the simulations, this was generally chosen as the limit below which the results from the group finder became significantly incomplete, and the structural parameters of subhaloes unreliable. In fact we expect resolution effects to remain important at much larger masses. As discussed in Diemand et al. (2004a), the mean relaxation time for cuspy systems with density profiles similar to those of subhaloes is less than a Hubble time when they are resolved with a few hundred or even a thousand particles. Furthermore, this calculation assumes present-day densities (e.g. a half-mass radius of 24 kpc for a system of mass  $3.5 \times 10^9 M_{\odot}$ , versus  $\sim 20$  kpc for an isolated halo of the same mass at  $z = 0$  in our model). For systems which formed at redshift  $z$  the relaxation time should be shorter by a factor  $(1+z)^{3/2}$ . Thus we also include shorter lines showing a 320-particle mass, below which most systems should be artificially relaxed.

In each case, the cumulative mass function is roughly a power-law at intermediate masses. The slope of the mass function differs substantially between the two simulations, however – it is about  $-0.96$  for Virgo IIb and  $-1.31$  for Coma, as indicated by the dotted lines. A priori, it is not clear whether this difference is due to intrinsic, halo-to-halo variation in the mass function, the different masses of the two systems, their redshifts or their different internal dynamical states, or whether it is the result of different softening and mass resolution. The latter seems unlikely given the large difference even for well-resolved ( $10^3$ – $10^4$ ) subhaloes. From the discussion in paper II, it seems likely that dynamical age is an important factor. The progenitor of the ‘Coma’ halo formed in isolation and was fully relaxed at  $z = 0$  (M98), while Virgo IIb, at a redshift of 0.1, contains massive subsystems that have not yet been stripped or disrupted to the same degree.

We also see in this figure that at low masses, the cumulative mass function deviates from a power-law well before the 32-particle limit of the group-finder is reached, but somewhere in the 100–300 particle range below which relaxation may be important. Here again, though, it is not clear how much of the curvature of the mass function is real and how much is numerical. We will discuss this further when we compare these results to the semi-analytic predictions.

<sup>1</sup> In the case of the ‘Local Group’ haloes, the mass of the main halo was measured at  $z = 0$ , whereas our outputs are for  $z = 0.2$ . We have assumed that the halo masses were 0.885 of their final value at this redshift, based on the average accretion rate measured in our merger trees. The virial radius for an object of a given mass is also smaller at  $z > 0$ , since it is defined in terms of a fixed overdensity relative to the background.



**Figure 2.** Cumulative relative mass and velocity distributions from various simulations of haloes on cluster (top panels) and galaxy (bottom panels) scales. The top left-hand panels show the cumulative mass functions for Virgo I (dotted line) and Virgo IIa & IIb (solid and dashed lines), while the bottom left-hand panel shows the relative mass function for Andromeda (solid line) and the Milky Way (dotted line). The bottom axis shows mass relative to the virial mass, while the top axis shows the mass scaled to our fiducial halo. A line of slope  $\alpha$  is also shown on each plot. The vertical lines indicate the 32-particle and 320-particle mass-resolution limits for each simulation, and the right-hand panels show cumulative distributions of peak circular velocity for Virgo IIa & IIb (top right) and for the Local Group (bottom right), as well as lines of slope  $\beta$ . The bottom axis gives the value relative to the virial velocity of the main halo, while the top axis gives the velocity scaled to our fiducial system.

### 3.2.2 Dependence on halo mass

We can test whether the mass function depends on halo mass in a simple way by comparing results for galaxy and cluster haloes. Fig. 2 shows the relative mass functions for all the simulations of Virgo-sized haloes (top left panel), as well as the mass functions for the two galaxy-sized haloes (bottom left panel). The top axis indicates the equivalent subhalo mass and circular velocity in our fiducial system (i.e. for  $M_{\text{vir},m} = 1.6 \times 10^{12} M_{\odot}$ ). The vertical lines indicate a 32-particle and a 320-particle lower mass limit in each simulation.

All five scaled mass functions are similar, although both the normalisation and the slope vary by  $\sim 20$  percent. The variation in normalisation depends on our convention for rescaling the distributions; if we were to count all the haloes within  $1.5 r_{\text{vir},m}$ , for instance, then Andromeda would have more satellites than the Milky Way. We will only count subhaloes within  $1.0 r_{\text{vir},m}$ , however, as the semi-analytic results are incomplete beyond this point, as explained previously.

The variation in slope is also hard to define precisely, since the mass functions deviate from a power-law at both large and small masses, either for physical reasons or for

numerical ones. Still, there is a significant difference between the two sets of mass functions. The thin solid lines show a rough fit to the slope of the mass function at intermediate mass, with the logarithmic slope  $\alpha$  indicated on the plot. The trend in the slope going from galaxies to clusters is the opposite of the one in Fig. 1, in the sense that the less massive systems have steeper mass functions, so it cannot be explained simply in terms of halo mass. Instead it may reflect the dynamical ages of the different systems, as discussed above and in paper II. In this case, the Local Group haloes would be systematically older than Virgo, just as Coma is.

Similar results have been reported recently for  $\Lambda$ -CDM simulations. De Lucia et al. (2004), for instance, find logarithmic slopes of  $-0.97$  to  $-0.98$  for the mass function on cluster scales, and  $-1.11$  to  $-1.13$  on galaxy scales (although the quantity they fit is  $dn(M)/d(\log(M))$  versus  $\log(M)$ , for power law distributions the slope of this quantity has the same numerical value as the logarithmic slope of the cumulative distribution  $\alpha$ ). The trend to steeper slopes for smaller haloes is as in Fig. 2.

### 3.2.3 Shape of the cumulative velocity distribution

The right-hand panels of Fig. 2 show the cumulative distributions of peak velocity, either relative to the virial velocity of the main system (bottom axis), or scaled by our fiducial value of  $148 \text{ km s}^{-1}$  (top axis). These are also well described by power-laws at intermediate mass, as indicated by the thin solid lines. The logarithmic slope  $\beta$  is indicated on the plot. For self-similar haloes we expect  $v_p \propto M^{1/3}$  and therefore  $\beta = 3\alpha$ ; in practice the slope seems slightly steeper than this, perhaps indicating that the small subhaloes are more concentrated than the large ones. The velocity distributions show stronger deviations from a power-law at small velocities than the mass functions do at low masses; we will discuss a possible explanation for this in section 4.2.

Finally, we note that these mass and velocity distributions are similar to, and consistent with, others that have appeared in the literature (e.g. Klypin et al. 1999b; Okamoto & Habe 1999; Springel et al. 2001; Governato et al. 2001; Stoehr et al. 2002; De Lucia et al. 2004; Desai et al. 2004; Gill et al. 2004a; Diemand et al. 2004c; Gao et al. 2004b; Weller et al. 2004; Reed et al. 2004; Nagai & Kravtsov 2004). In particular,  $\Lambda$ CDM haloes appear to have almost identical substructure, consistent with the results of paper II, and the intrinsic variation in the cumulative distributions from one halo to another are similar to those reported here.

## 4 COMPARISON BETWEEN NUMERICAL AND SEMI-ANALYTIC RESULTS

### 4.1 Cumulative distributions

We now turn to the comparison between numerical and semi-analytic results. We will consider results for the dense inner regions of the halo and the lower-density outer regions separately, since numerical effects may affect the former to a greater degree, as discussed in section 4.3 below. The right-hand panel of Fig. 3 shows the cumulative mass function, for all substructure between  $0.5$  and  $1.0 r_{\text{vir},m}$  from the centre or each halo. Over this range of radii, our model reproduces

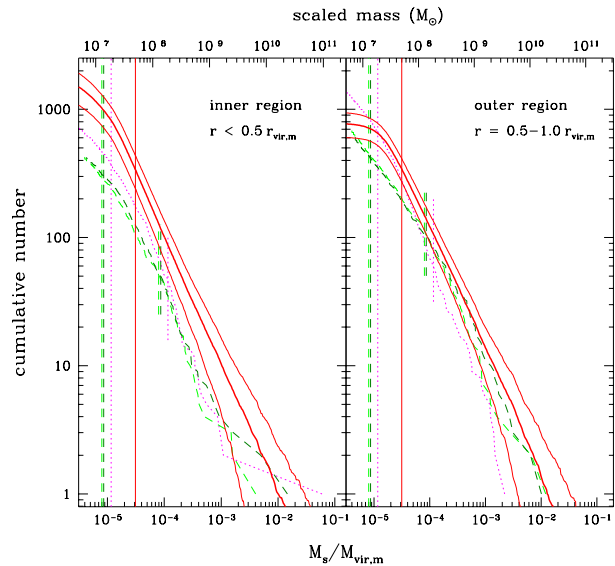


**Figure 3.** The cumulative mass function predicted by the semi-analytic model, in the inner (left-hand panel) and outer (right-hand panel) parts of the halo. The thick lines show the average result for a hundred SCDM merger trees, for model B at  $z = 0$ . The thin solid lines show the  $1\text{-}\sigma$  variance for this set. The thin lines are the normalised cumulative mass functions measured in the three highest-resolution simulations (dashed lines – Virgo IIa and IIb; dotted lines – Coma). The vertical dotted and dashed lines indicate the 32-particle and 320-particle resolution limits of the numerical results. The solid vertical line indicates the resolution limit of the semi-analytic trees.

the numerical results almost exactly, both in normalisation and in scatter. For massive haloes, the cumulative distribution in the semi-analytic haloes is very similar to those in the high-resolution simulations. All three simulations lie below our average value, but the offset is a small ( $\sim 20$  percent, or about equal to the halo-to-halo scatter, on average), so it may not be significant. There are several effects such dynamical age that could explain this offset, but we do not expect our prescription for mass loss to be accurate to much better than 10–20 percent in any case, as discussed in paper I.

At smaller masses ( $M_s < 10^{-4} M_{\text{vir,m}}$ ), the semi-analytic model predicts 30–40 percent more substructure above a given mass threshold. It seems likely that at least some of this offset is due to numerical effects such as relaxation, since here we are below the limit of a few hundred particles where the relaxation time becomes shorter than the Hubble time (Diemand et al. 2004a). Overall we conclude that in the outer part of the halo, where the properties of substructure are most robustly determined in the simulations, the two sets of results are in acceptable agreement.

On the other hand, in the region interior to  $0.5 r_{\text{vir,m}}$  (left-hand panel), the semi-analytic mass function predicts roughly 2.5 times more substructure above a given mass threshold than is seen in the numerical simulations. In terms of the halo-to-halo scatter, all three numerical mass functions lie  $2\sigma$  below the average value in the semi-analytic trees. The cumulative velocity functions (Fig. 4) show a sim-

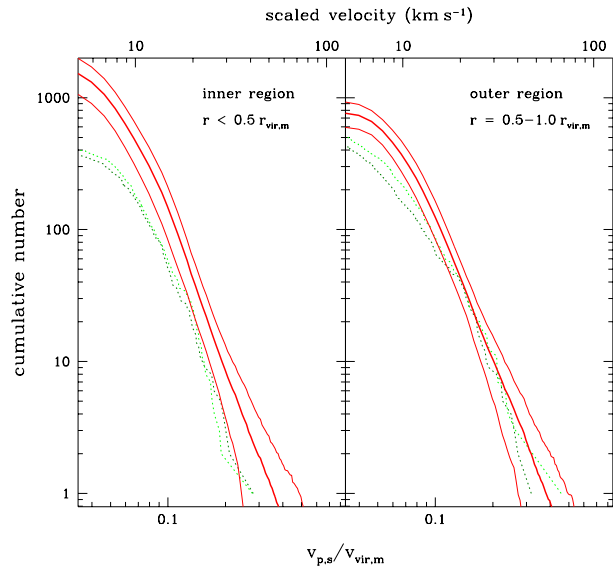


**Figure 4.** The cumulative peak circular velocity functions predicted by the semi-analytic model. The left-hand panel shows results for haloes within half the virial radius; the right-hand panel shows results for haloes between 0.5 and  $1 r_{\text{vir,m}}$ . The thick lines are the average result and  $\pm 1\text{-}\sigma$  contours for a hundred SCDM merger trees, for model B at  $z = 0$ . The thin lines are the normalised cumulative velocity functions measured in the Virgo IIa and IIb simulations.

ilar pattern. This suggests that the two methods disagree significantly about how quickly substructure is stripped or destroyed in the central regions of a halo. Unfortunately, it is not clear which result is more accurate. As seen in paper II, central subhaloes are generally older and they will have experienced more mass loss and tidal heating on average, having orbited many times in a strong and changing potential. Since many of these central systems will be heavily stripped, the semi-analytic predictions about their residual bound mass be less accurate than for younger systems. On the other hand, the simulations will also be less accurate for old systems and at small radii, due to the cumulative effects of relaxation and artificial heating. Moreover, it is harder for group finders to identify substructure correctly in dense regions (Gill et al. 2004a), and the subhalo masses and velocities they determine in these regions can be biased by the background density. Thus it may be that semi-analytic predictions for substructure are in fact *more* accurate than simulations in the centres of halos (say within  $0.3 r_{\text{vir,m}}$ ). We will discuss this further in section 4.3.

## 4.2 Individual subhaloes and the role of softening

We can also compare the properties of individual haloes directly. Fig. 5 shows a comparison of the semi-analytic subhaloes (left-hand plots) and the numerical subhaloes (right-hand plots), in terms of their mass and their peak circular velocity. The numerical results, from top to bottom, are from the Milky Way, Andromeda, Virgo IIb, and Virgo IIa haloes. The masses and velocities in the simulations have all

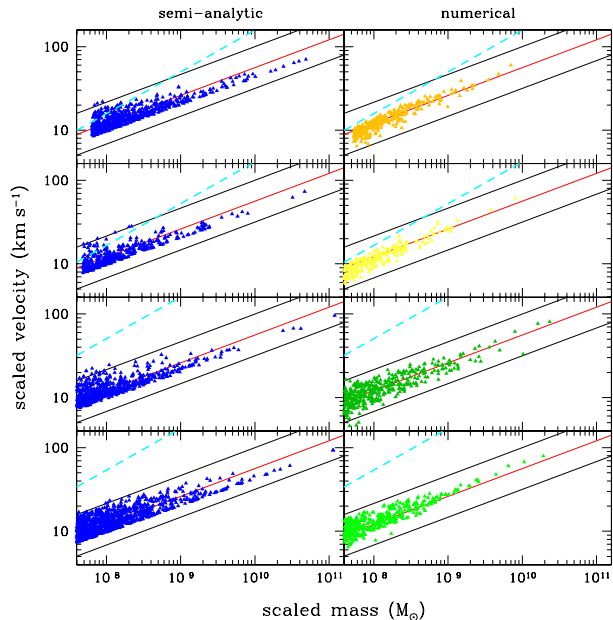


**Figure 5.** The distribution of subhaloes as a function of their mass and of their peak velocity, in the semi-analytic model A (left-hand plots) and the simulations (right-hand plots). The numerical values have been scaled to the mass and circular velocity of the main halo (see text). The dashed lines indicate the regions of the plot excluded by softening.

been rescaled to the mass and velocity of the parent halo in the semi-analytic model, as explained in section 3.1, and in each pair of panels we have only plotted systems above the mass-resolution limit of the numerical data in the right-hand panel.

Overall, the distributions seem remarkably similar. Comparing them in detail, however, we note some minor differences. The semi-analytic model predicts the existence of low-mass, high-density (high- $v_p$ ) systems, for instance, which are not seen in the simulations. This is partly because the forces in the simulation are softened over a finite length  $r_s$ , such that the potential generated by a set of particles of mass  $M$  is limited to  $\simeq GM/r_s$ , placing a corresponding limit on  $v_p$ . The dashed lines in each of the left-hand panels indicate the locus of this limit, for the values of  $r_s$  listed in table 1. As expected, none of the numerical subhaloes lie above this line, whereas we might expect some to in the low-resolution simulations (upper two panels). The high-resolution simulations (lower two panels) fall well short of this limit, although they may be still subject to relaxation and other effects.

We also see that the numerical distributions generally extend to lower circular velocities at a given mass than the semi-analytic distributions. This may be partly due to softening, but another explanation is shot noise in the particle distribution for these systems. Low mass haloes will have few particles interior to  $r_p$ , so subtracting a single particle from a halo can reduce its peak velocity substantially. This may explain the greater scatter in the lower left-hand corner of each of the numerical distributions.

We can model the effect of softening explicitly by assuming that the circular velocity is determined by the ra-

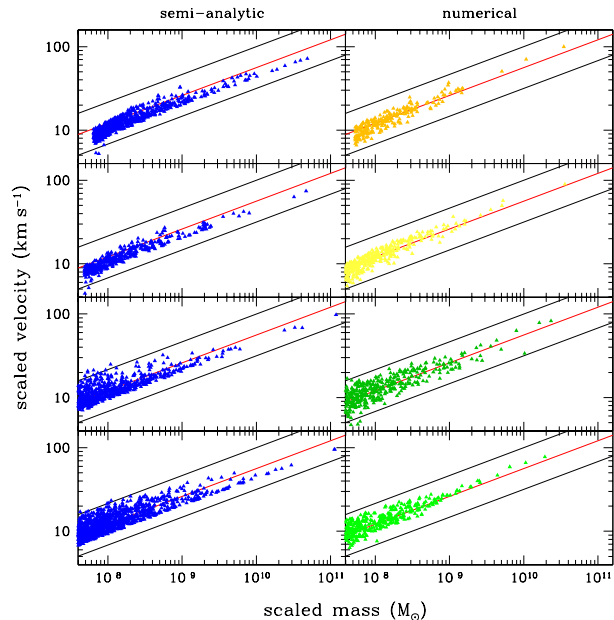


**Figure 6.** As Fig. 5, but including some of the effects of force softening and mass resolution in the semi-analytic results (left-hand panels).

dial force,  $v_c = r\dot{F}_r$ , and using the force softening to reduce  $v_c$  accordingly. The forces in these simulations were spline softened, that is the potential generated by each particle was calculated as  $\Phi = \Phi_s(r/r_s)$ , where  $\Phi_s$ , the softened potential, is a polynomial  $P_1(r/r_s)$  for  $0 \leq r \leq r_s$ , a polynomial  $P_2(r/r_s)$  for  $r_s \leq r \leq 2r_s$ , and equal to the Newtonian potential beyond this (where  $r_s$  is the softening length of the simulation). We can account for this by reducing the radial force accordingly; this reduces the peak velocity when  $r_p$  is close to the softening length  $r_s$ . To simulate shot noise, we can assume that the number of particles within  $r_p$  varies randomly by  $\sqrt{N}$ , thereby introducing a scatter into haloes where  $M(< r_p)$  is close to  $m_p$ , the particle mass. Fig. 6 shows the distribution of velocities and masses, with both shot noise and softening taken into account. We see that our modified distributions are now very close to those found in the simulations, particularly at low resolution.

Finally, we can re-examine the cumulative velocity function with softening taken into account. Fig. 7 shows the cumulative (peak circular) velocity function for subhaloes, with line styles as before. The semi-analytic results have been softened as in Fig. 6, with a softening length corresponding to that used in the simulations shown. The upper panels are for the higher-resolution Virgo II simulations, in which the softening length was  $r_s = 0.0005 r_{\text{vir},m}$  (or 170 pc in our fiducial system), while the lower are for the Local Group simulations, in which the softening length was roughly  $r_s = 0.005 r_{\text{vir},m}$  (or 1.7 kpc in our fiducial system). As before, the semi-analytic predictions match the simulations reasonably well in the outer parts of the halo, but predict 2–3 times more substructure above a given velocity threshold in the inner parts. Comparing the upper and lower panels, we see that softening alone may account for most of the difference between the high-resolution and low-resolution numerical results in the amplitude of the cumu-

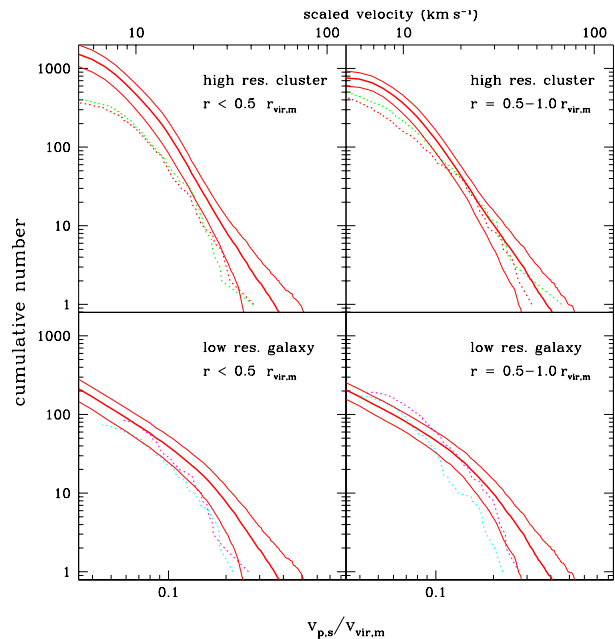


**Figure 7.** Average cumulative peak circular velocity functions predicted by the semi-analytic model, including the effects of softening. Merger trees and line styles are as in Fig. 4. The softening length in the upper panels,  $r_s = 0.0005 r_{\text{vir},m}$ , is comparable to that in the Virgo IIa and IIb simulations (dotted lines), while the lower panels show similar results using a softening length of  $0.005 r_{\text{vir},m}$ , along with the normalised Local Group distributions (dotted lines).

relative velocity function below  $v_s/v_{\text{vir},m} \sim 0.15$ . The match between the softened semi-analytic predictions and the simulations is still not exact, however (e.g. the disagreement in the amplitude of the mass function at  $r < 0.5 r_{\text{vir},m}$ ), suggesting there may be other resolution effects we have not considered.

Indeed, there are several well known sources of artificial heating in  $N$ -body simulations that we have not accounted for so far. Internal relaxation will reduce the mass, circular velocity and potential of each subhalo artificially, on a timescale roughly proportional to the number of particles. For systems resolved with fewer than  $\sim 300$  particles, this timescale is shorter than the Hubble time, as mentioned previously, so only the youngest objects will be unaffected by relaxation. The ‘graininess’ of the background potential will also heat systems artificially, particularly at early times when the main halo is poorly resolved. These effects have been studied extensively in the literature in the context of the ‘overmerging problem’, as discussed in the next section.

### 4.3 Spatial distributions and the evidence for overmerging

#### 4.3.1 Radial distributions compared

The results of section 4.1 suggest that the simulations may underestimate the amount of substructure in the central regions of haloes. In early simulations, the dissolution of substructure within haloes, referred to as ‘overmerging’, rendered simulated systems almost completely smooth (see van Kampen 1995; Moore, Katz, & Lake 1996; or Klypin et al.

1999a for discussions of the problem). Overmerging is known to occur to some degree even in high-resolution simulations (Ghigna et al. 2000), and should be strongest in the old, dense central regions of haloes (Diemand et al. 2004a). The results of section 4.1 suggest that it could still be important over a fairly large range of radii.

We can quantify the effects of overmerging by comparing the radial distribution of substructure in our model and in the simulations. The top three panels of Fig. 8 show the local density of subhaloes at a given radius, relative to the mean density within the virial radius,  $n(r)/\bar{n}_{\text{vir},m} = (N(<r)/dV(r))/(N_{\text{vir}}/V_{\text{vir}})$ . The connected points with error bars show the results in three simulations, and the upper solid lines show the predictions of semi-analytic models A and B. We saw in paper II that the radial distribution of subhaloes is biased by incompleteness if we go below the mass resolution limit of the merger tree. To avoid this bias, the semi-analytic results shown in the left and middle panels include only systems with masses in excess of  $5 \times 10^7 M_{\odot}$ , while the numerical results are limited to an equivalent relative mass range,  $M_s/M_{\text{vir},m} > 3 \times 10^{-5}$ . The resolution limit of the ‘MW’ simulation is actually worse than this, so in the right-hand panel we cut both the numerical and the semi-analytic results at  $10^8 M_{\odot}$ . The dashed line shows a Moore density profile of concentration  $c_M = 5.4$  (roughly appropriate for galaxy or cluster mass haloes), also normalised to the mean density within the virial radius. We note that similar numerical results have been presented recently by several authors (Gill et al. 2004a; Diemand et al. 2004c; Gao et al. 2004; Reed et al. 2004; Nagai & Kravtsov 2004).

The local density profile has the disadvantage of being quite noisy in the central regions of the halo, and its overall appearance depends partly on the choice of radial bins. In the bottom panels, we therefore show the cumulative number of subhaloes within a given fraction of the virial radius, normalised to the total number within the virial radius, since this quantity is monotonic and requires no binning. The mass cuts are the same as in the top panel, and the dashed lines show the mass of the main halo interior to a given radius, normalised to the mass within the virial radius.

Both numerical and semi-analytic models agree that subhaloes are antibiased with respect to the underlying density distribution, and both agree on the distribution in the outer parts of the halo, at  $r > 0.3 r_{\text{vir},m}$ . In the central region, however, the semi-analytic model predicts a substantial excess of subhaloes compared to the simulations –  $n(r)/\bar{n}_{\text{vir}} \sim 20$  at  $0.1 r_{\text{vir},m}$  and  $\sim 10$  at  $0.2 r_{\text{vir},m}$ , whereas in Virgo IIa the values are  $\sim 7$  and  $\sim 5$  respectively. As an indication that the semi-analytic result is robust, we see that the excess depends only weakly on the disruption criterion used (the upper and lower semi-analytic curves correspond to models B and A respectively). On the other hand, with increasing resolution (three panels, right to left) the numerical distributions gradually become more concentrated, approaching the semi-analytic results in the highest-resolution case. Thus it seems likely either that overmerging is still important in the inner regions of the simulated haloes, or that the group finders used to generate the numerical datasets have missed substructure in the central regions. We will discuss this further in section 4.5.

Overmerging at the level we are suggesting should also



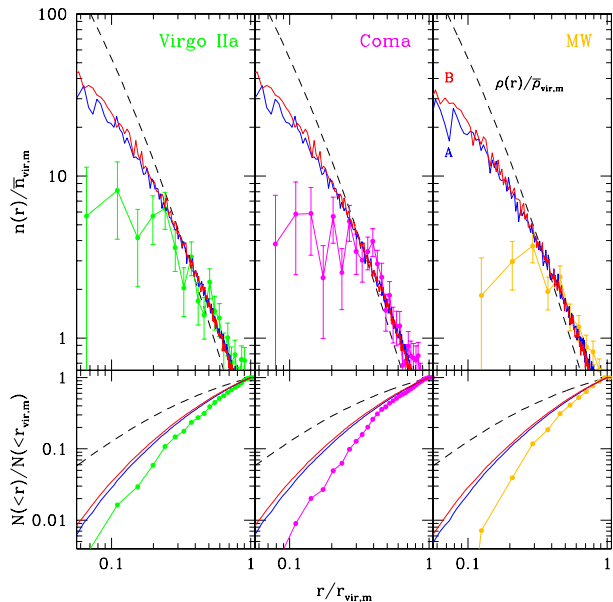


**Figure 8.** Top panels: The number density of subhaloes in three simulations (connected points with error bars), and in the semi-analytic haloes (upper solid lines), for models A and B. To avoid incompleteness, the semi-analytic results include only systems with masses in excess of  $5 \times 10^7 M_\odot$  (left and middle panels) or  $10^8 M_\odot$  (right panel), and the numerical results have been restricted to the same relative mass range. In each case the density is relative to the mean number density within the virial radius. The dashed line shows the density profile of the main halo, normalised to the mean density within the virial radius. Bottom panels: The cumulative number of subhaloes vs. radius, normalised to the number within the virial radius, for the same mass cuts as in the top panel. The dashed lines show the mass of the main halo interior to a given radius, normalised to the mass within the virial radius.

reduce the amplitude of the cumulative mass function within the virial radius, but the overall effect will be small, because even in our semi-analytic models, relatively few subhaloes are found at small radii. Since the semi-analytic model predicts that only 25–30 percent of all haloes within the virial radius are at radii of  $0.2\text{--}0.3 r_{\text{vir},m}$  or less, the change in the amplitude of the mass function would only be 25–30, even if overmerging destroyed all objects in these regions. This may explain why simulations have previously shown good convergence in the cumulative distributions of subhaloes within the virial radius as a function of resolution (e.g. Springel et al. 2001; Diemand et al. 2004c; Gao et al. 2000b). These distributions are dominated by subhaloes relatively far from the centre of the potential, which are less influenced by numerical effects, and thus they will not be sensitive to central overmerging.

On the other hand, it seems more surprising that convergence studies have seen no major change in the radial distribution of substructure (Diemand et al. 2004c; Nagai & Kravtsov 2004). This may be partly due to the obscuring effects of halo-to-halo scatter, halo concentration or binning, which make it difficult to identify statistically significant differences between two density distributions. It may also be

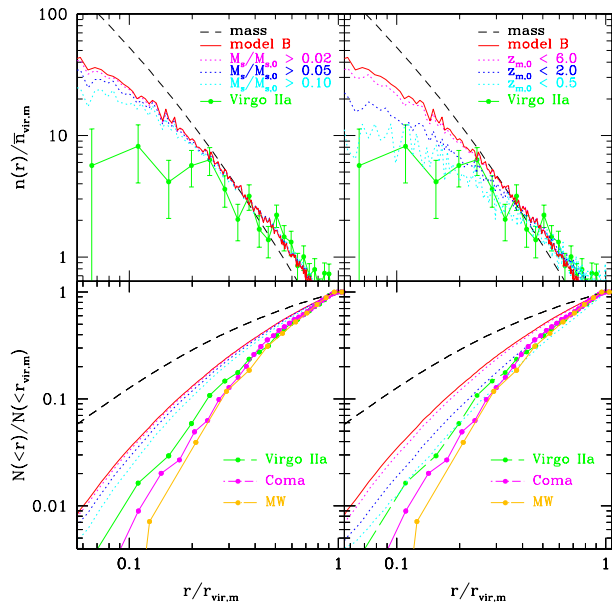


**Figure 9.** As Fig. 8, but for various cuts in subhalo properties. The left-hand panels show the results of ignoring all subhaloes stripped beyond some fraction of their original mass (dotted lines); the right-hand panels show the results of ignoring all systems the formed before a given epoch (dotted lines).

that the convergence in the radial distribution of substructure is very slow; we will discuss this further in section 4.5.

#### 4.3.2 Results for variant models

Overmerging of the magnitude suggested by these results would have important implications in many astrophysical situations, notably the interpretation of strong lensing observations and direct detection experiments. Thus, it is interesting to consider how strongly these results could be affected by uncertainties in the semi-analytic modelling. We have compared number density profiles for the variants of the model considered in paper II with our fiducial results. While the profiles change in predictable ways (e.g. more dynamical friction or less mass-loss produces more central substructure over a given mass threshold), the variation is generally comparable to the difference between models ‘A’ and ‘B’ shown in Fig. 8.

On the other hand, it might be that our analytic mass-loss model systematically underestimates mass loss in systems that have been heavily stripped. To get a sense of how large an effect is required to reproduce the numerical results, we have calculated number density profiles excluding systems that retain only 2 percent, 5 percent, or 10 percent of their original mass. These are shown in the left-hand panels of Fig. 9 (dotted lines), along with the profiles from the three simulations (solid lines with points – note the mass resolution limit for the Milky Way results is higher) and the fiducial results for model B (uppermost solid line). We see that even if we treat as disrupted all systems that have lost 90 percent of their mass, we still produce more central substructure than the highest-resolution simulation, albeit only by a factor of 2 or so. The results of Hayashi et al. suggest

that bound cores can survive in systems that have lost 99 percent of their mass or more, so it seems unlikely that our mass-loss predictions are incorrect to a degree sufficient to resolve the discrepancy with the numerical results.

We can also get a feel for the plausibility of substantial numerical overmerging by considering *how long* subhaloes have orbited within the main system. The right-hand panels of Fig. 9 show number density profiles excluding the oldest subhaloes, those that first formed at redshifts of more than 6.0, 2.0 or 0.5 (dotted lines). As expected from the results of paper II, substructure is stratified with respect to its age, so the central substructure we predict in excess of that found in the simulations is mainly old – almost all of the central systems formed before a redshift of 0.5, when the universe was roughly half its present age, and most formed before  $z = 2$ , when the universe was less than 20 percent of its present age. This material would have undergone many orbits in the dense central regions of the main system or its progenitors, so it seems very plausible that artificial numerical heating could have caused it to disrupt prematurely. We will reformulate this argument more precisely in the next section. Finally, we note that while the radial distributions of substructure do vary systematically from one halo to another if we bin haloes by their formation epoch, as in paper II, the variation is generally small (comparable to the difference between models A and B).

#### 4.4 Subhalo kinematics

If overmerging is important, it will also affect the distributions of other subhalo properties. Fig. 10 compares the kinematics and dynamical state of subhaloes in the semi-analytic and numerical models. The top two panels in each column show subhaloes from two different semi-analytic haloes; the third panel shows all subhaloes from the second of these that formed at  $z_{m,0} < 2$ , and the bottom panel shows subhaloes from the Virgo IIa simulations. For the semi-analytic results, open symbols represent systems that have lost more than 90 percent of their original mass, while the symbol shape indicates formation epoch (triangles:  $z_{m,0} < 0.5$ ; squares  $z_{m,0} = 0.5\text{--}2.0$ ; circles  $z_{m,0} > 2.0$ ). In each case, all subhaloes within the virial radius and over a mass limit of  $10^{-5}M_{\text{vir},m}$  are included.

The left-hand column shows velocity versus orbital circularity. In paper I, we discussed the initial and final circularity distributions in our model. As Fig. 10 shows, the final circularity and velocity distributions for a semi-analytic system and the Virgo IIa subhaloes are very similar. Given that the orbital properties of subhaloes in the semi-analytic model are the result of a complex superposition of several effects, including the initial energy and angular momentum distributions, dynamical friction, selective disruption and the growth of the main halo, this agreement is very encouraging.

The middle column shows velocity versus position. Both in the semi-analytic and in the numerical results, the distribution is bounded by the same well-defined upper limit at any given radius. The line indicates that this boundary is roughly  $v_{\text{max}}(r) = v_{\text{vir},m}(r/r_{\text{vir},m})^{-1/3}$  down to  $r/r_{\text{vir},m} = 0.1$ . The semi-analytic model clearly predicts more substructure in the central regions, and thus a higher central velocity dispersion for the subhaloes as a group.

Finally, the right-hand column shows orbital energy versus position. The overall distributions are very different, the semi-analytic model predicting many more very strongly bound subhaloes. Most of these systems are very old, however, and disappear if we restrict the sample to systems that formed after  $z = 2$  (third panel from the top). Thus we see the same effect discussed in the previous section, namely that the older systems predicted in the semi-analytic models are absent in the numerical results.

#### 4.5 Comparison with semi-analytic results: summary

In summary, in this section we have used a set of high-resolution simulations to estimate the average properties of halo substructure, as well as the intrinsic scatter from one halo to the next, and the variation with halo mass or concentration. Comparing these simulations with the predictions of our semi-analytic model, we find that while there is an overall similarity in the results, the level of agreement depends on the location, mass and age of the subhaloes.

##### 4.5.1 The outer halo

In the case of intermediate or high-mass subhaloes in the outer regions of the halo, for which the numerical results are expected to be most reliable, the agreement between the two methods is excellent; the cumulative mass and velocity distributions of the three high-resolution simulations all lie within 1–2 times the halo-to-halo scatter of the average value predicted by the semi-analytic model, and the overall difference between the average semi-analytic and numerical results is less than 20 percent.

Assuming this offset is significant, there are several effects that could introduce systematics at this level. Possible effects in the semi-analytic model include the various approximations in the dynamical component of the model, harassment between subhaloes (cf. paper II), or the preferential selection of haloes with older or younger formation epochs. On the latter point, we note that the simulations discussed here generally selected relaxed systems from larger volumes to study at high resolution; thus they do not constitute an unbiased sample of the dark matter haloes in a given mass range. The Virgo simulations, for instance, were of a cluster that had acquired 80 percent of its final mass by a redshift of 0.75, which is unusual for an object in this mass range (G98, Fig. 3). We can see from paper II, Fig. 14 that if we were to select out the oldest merger trees from our sets of semi-analytic haloes, we would obtain an even closer match to the simulations.

Possible effects in the numerical results include softening, shot noise, or problems with the group finder, all of which change the interpretation of the results from a single output of the simulation, as well as some more serious problems, notably two-body relaxation, which actually modify the dynamics of simulated systems. The increased offset between the semi-analytic and numerical results at small masses may indicate the greater importance of these effects in poorly-resolved systems. Overall, however, we conclude that for intermediate or high-mass subhaloes in the outer regions of the halo, the two methods are consistent with

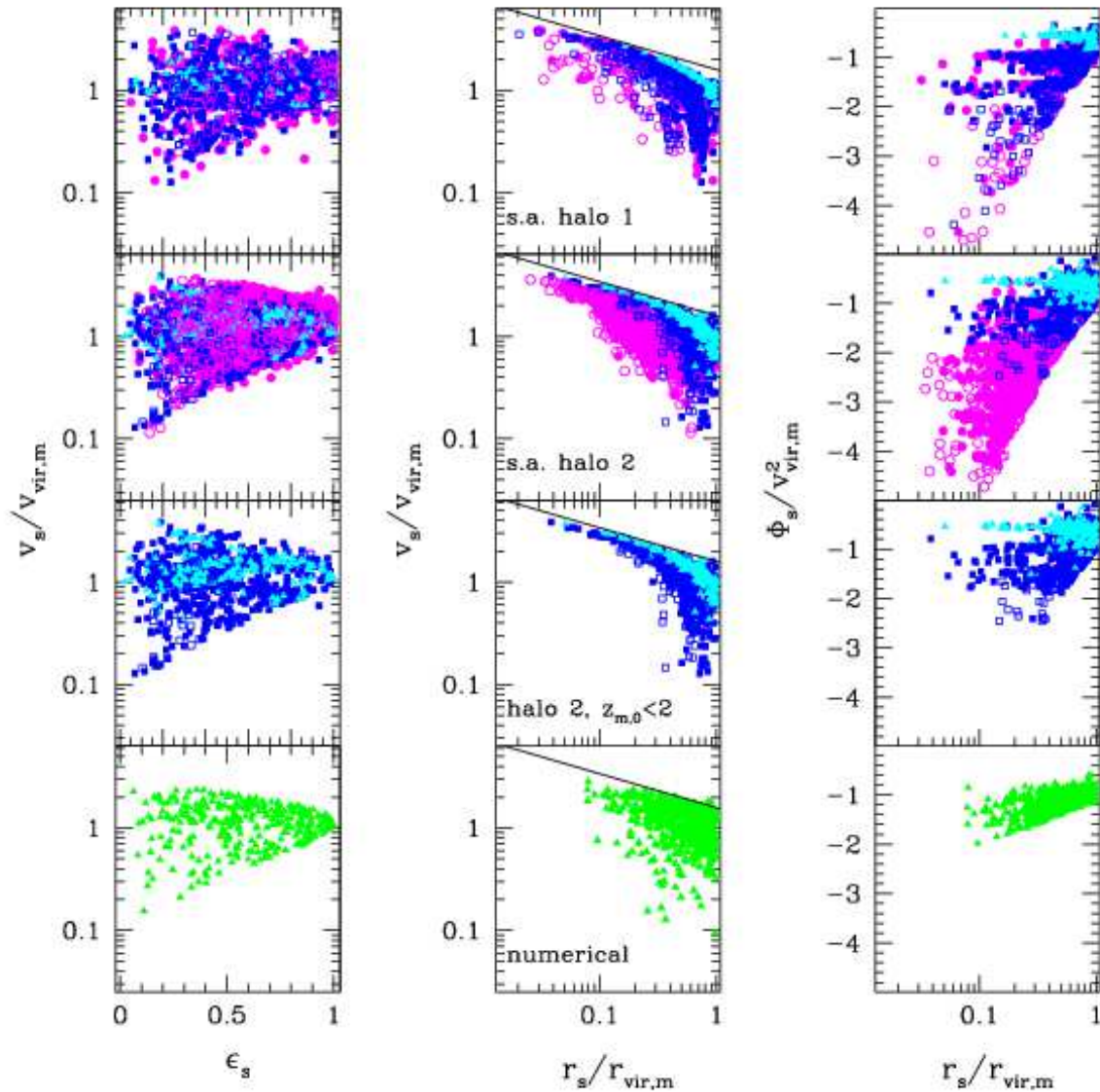


**Figure 10.** Kinematics and orbital parameters for subhaloes in two different semi-analytic haloes (model B; first and second panels in each column), subhaloes from the second of these that formed after  $z = 2$  (third panel), and subhaloes in the Virgo IIa simulations (bottom panels). The left-hand column shows velocity vs. circularity; the middle column shows velocity vs. position, and the right-hand column shows orbital energy vs. position. For the semi-analytic results, open symbols represent systems that have lost more than 90 percent of their original mass, while the symbol shape indicates formation epoch (triangles:  $z_{m,0} < 0.5$ ; squares  $z_{m,0} = 0.5\text{--}2.0$ ; circles  $z_{m,0} > 2.0$ ). In each case, all subhaloes within the virial radius and over a mass limit of  $10^{-5}M_{\text{vir},m}$  are included.

each other to good accuracy. We note that this agreement is achieved without adjusting any free parameters – the parameters in the semi-analytic model have all been fixed previously by other considerations, as discussed in paper I.

#### 4.5.2 The inner halo

On the other hand, in the inner regions of the halo, where numerical effects may be stronger, the semi-analytic model predicts substantially more substructure than the simulations. Some of this difference can be attributed to the same numerical effects mentioned above, but the net effect is that

the central regions of haloes appear to suffer from a fair amount of overmerging.

The possibility of central overmerging and the spatial distribution of substructure in numerical simulations have been investigated by a number of authors in more recent simulations (Gill et al. 2004a; Diemand et al. 2004c; Gao et al. 2004; Reed et al. 2004; Nagai & Kravtsov 2004). On the one hand, convergence studies using a given code and group finder find little or no evidence for a rapid increase in the amount of central substructure as the resolution increases (e.g. Diemand et al. 2004c; Nagai & Kravtsov 2004). This might seem a conclusive argument against overmerging.

ing, since increased resolution is the only way of testing for this possibility definitively.

On the other hand, detailed studies of the convergence of a different feature of halo structure, the slope of the central density profile, have found that the size of the region flattened by resolution effects such as relaxation decreases very slowly as the number of particles in the halo  $N$  increases, scaling as  $N^{-0.2}$ – $N^{-0.3}$  (Diemand et al. 2004a). This sort of scaling would be expected if the size of the unresolved region depends the mean inter-particle separation, for instance, or on the maximum density allowed by softening.

Resolving substructure in a dense background environment represents a similar, but harder, numerical problem. Not only does finite resolution limit the density of structures that can be resolved, but subhaloes are intrinsically less stable than a central cusp, since they are subject to much stronger tidal forces. Thus we should not expect to be able to resolve substructure at densities or on spatial scales where the central cusp of the main halo is flattened by relaxation, and in general the size of the region where substructure is artificially erased by relaxation should decrease no faster than  $N^{-1/3}$  as the number of particles  $N$  increases.

#### 4.5.3 How large is the unresolved region?

We can apply this argument more specifically to the numerical results presented here. The Milky Way and Virgo IIa simulations agree in the distribution of substructure beyond  $\sim 0.3 r_{\text{vir}}$ , but disagree within this radius. Given that they differ in  $N$  by a factor of 5, we estimate that the Virgo IIa results are reliable to  $\sim 0.17 r_{\text{vir}}$ . Diemand et al. (2004b, Fig. 7) present results for 4 galaxy haloes simulated with 1–4 million particles each. At  $0.17 r_{\text{vir}}$  they find  $n(r)/\bar{n}_{\text{vir}} \simeq 10$ , consistent with the semi-analytic predictions and the Virgo IIa results, so this may well be the radius at which the numerical results have converged.

Diemand et al. (2004b, Fig. 2) also present even higher resolution results, for a cluster halo resolved with up to 14 million particles. By the same scaling argument, we would expect these to be reliable down to  $0.11 r_{\text{vir}}$ , but in fact they still see substantially less substructure at this radius than is predicted by our model ( $n(r)/\bar{n}_{\text{vir}} \simeq 4$ – $5$ , versus  $15$ – $20$  in our model). On the other hand, their results for this cluster differ by a factor of 2 with the results for their four galaxy haloes (for which  $n(r)/\bar{n}_{\text{vir}} \simeq 10$  at this radius). Thus it is unclear whether the shallower density profile is characteristic of the cluster mass scale as opposed to the galaxy mass scale, whether it is simply due to intrinsic halo-to-halo variation, or whether the numerical convergence is even slower than  $N^{-1/3}$ .

There are indications of the first of these possibilities in the results of De Lucia et al. (2004, Fig. 6) and Gao et al. (2004b, Fig. 11), who find that subhaloes follow a more centrally concentrated distribution in galaxy haloes than in cluster halos. With regards to the second possibility, Gill et al. (2004b, Fig. 7) show that the scatter in the number density profile can be a factor of 2 or more in amplitude, although all 8 of their haloes have steep inner slopes in the radial distribution of substructure. In any case, if the third explanation were correct and the convergence rate scaled

as  $N^{-0.2}$ , we would expect convergent results only beyond  $0.17 r_{\text{vir}}$ , so this could also explain the discrepancy.

Finally, we note that the algorithm used to locate and define substructure may have a large effect in and of itself. Weller et al. (2004), for instance, find quite different bound mass estimates for subhaloes depending on the criterion used for associating particles with substructure, while Gill et al. (2004a), obtain substantially different results for the radial distributions of subhaloes by ‘tracking’ halo particles from one step to the next. In particular, they find that in all 8 of their haloes, the radial density of subhaloes identified by ‘tracking’ continues to rise down to the smallest radii they consider,  $r \simeq 0.07 r_{\text{vir}}$  (cf. their Fig. 7). With this technique, 10 percent of the substructure they identify is located within the inner  $0.1$ – $0.2 r_{\text{vir}}$ , as in our semi-analytic model, whereas for a group finder using only information from a single timestep, they find the cumulative distribution reaches 10 percent at  $\sim 0.3 r_{\text{vir}}$ , as in the simulations considered here. Analysing the same halo with different group finders, they find that normalised density at  $0.1 r_{\text{vir}}$  varies by a factor of 4.

#### 4.5.4 Relaxation times for central subhaloes

There is a second argument that suggests that simulations may still be missing substructure in their central regions. We expect strong correlations between the age of subhaloes and their location within the main system (cf. paper II). Central subhaloes are systematically older, and if we artificially remove the oldest subhaloes from our semi-analytic results, we achieve a much better match to the numerical results (cf. Figs. 9 and 10). Central subhaloes typically formed at or before  $z = 2$ ; thus they were originally  $3^3 = 27$  times denser than present-day systems of the same mass, and have spent roughly 5 orbits or 11 Gyr in the main system (paper II, Fig. 8), losing 75 percent of their original mass in the process (paper II, Fig. 9).

On the one hand, the high-resolution simulations of H03 and Kazantzidis et al. (2004) indicate that low-density systems resolved with  $\sim 10^4$  particles can easily survive this degree of mass loss without disintegrating. On the other hand, when systems of the density corresponding to  $z_{\text{m},0} = 2$  are resolved with fewer than 5000 particles, their relaxation time is less than the Hubble time (Diemand et al. 2004). For systems of  $\sim 32$  particles, the nominal resolution limit of the numerical data sets, the relaxation time at this density is 100–200 Myr. While it is not clear how exactly quickly relaxation leads to the disruption of substructure, it seems unlikely that 32 particle systems merging at  $z = 2$  could survive for the equivalent of 50 relaxation times without being completely dissolved. This artificial disruption due to internal relaxation would have little effect on the overall properties of substructure averaged over the entire halo, since only a small fraction of all subhaloes are this old. On the other hand it would quickly reduce the central density of subhaloes, since the latter is dominated by small objects that formed at early times.

The preferential disruption of old subhaloes close to the centre of the main system has important implications for many of the observational tests of halo substructure. In section 5, we will consider two examples, the detection of

substructure in multiply-lensed systems, and the direct detection of dark matter in terrestrial experiments.

## 5 IMPLICATIONS FOR OBSERVATIONAL TESTS OF SUBSTRUCTURE

### 5.1 Implications for lensing

Gravitational lensing, the deflection of light from a background source by the gravitational potential of a foreground system, provides at least two ways of quantifying the amount of dense substructure in the halo of the lensing system. The dark matter around individual galaxies systematically distorts the shapes of background galaxies within some projected separation. In rich clusters, these distortions can be averaged over a large number of galaxies at the same redshift, yielding maps of the projected mass density within the cluster, and statistical information about the subhaloes around each cluster member (e.g. Natarajan, Kneib & Smail 2002; Gavazzi et al. 2004). The resulting mass maps cover a large fraction of the projected area of the cluster at high spatial resolution, but they are somewhat model-dependent. In particular, they require the presence of visible galaxies to trace the dark matter substructure.

There is an alternate lensing method that promises to reveal completely dark substructure in the haloes of galaxies. It consists of comparing the amplification ratios of different components in multiply-lensed systems with models of the mass distribution in the lens. For particular lens geometries, discrepancies in the amplification ratios may indicate a deviation from a smooth potential on the scale of the image separation. This method for quantifying substructure received much attention recently, with claims that the projected mass fraction contained in substructure had been measured fairly reliably for a set of systems (Dalal & Kochanek 2001, 2002), and that lensing statistics might be allowed the power spectrum to be constrained directly (Zentner & Bullock 2003).

In the light of subsequent work, these results now seem less certain. For many individual systems, various other effects including stellar microlensing (Schechter & Wambsganss 2002), scintillation, or biases in the lens modelling (Evans & Witt 2003) may be sufficient to explain the anomalous flux ratios. An improved method uses observations at many different wavelengths to eliminate the microlensing contribution, taking advantage of the fact that microlensing and lensing by substructure should have different effects on the broad-line and narrow-line regions of lensed AGN, due to their different spatial scales (Moustakas & Metcalf 2003; Metcalf et al. 2004). On the other hand, even this method cannot prove that the small-scale structure is actually within a given halo, rather than simply being seen in projection (e.g. Chen, Kravtsov, & Keeton 2003; Metcalf 2004). In the longer term, ultra-high resolution images from very long baseline interferometry (Inoue & Chiba 2003) or novel techniques with X-ray telescopes (e.g. Yonehara, Umemura, & Susa 2003) in space may produce more conclusive detections of halo substructure.

Whatever the status of the problem observationally, it is not clear that there is a robust theoretical prediction with which to compare current observational results. Strong lensing probes the mass fraction in relatively low-mass substructure ( $10^5 M_\odot$ – $10^7 M_\odot$ ), in the central few kiloparsecs of

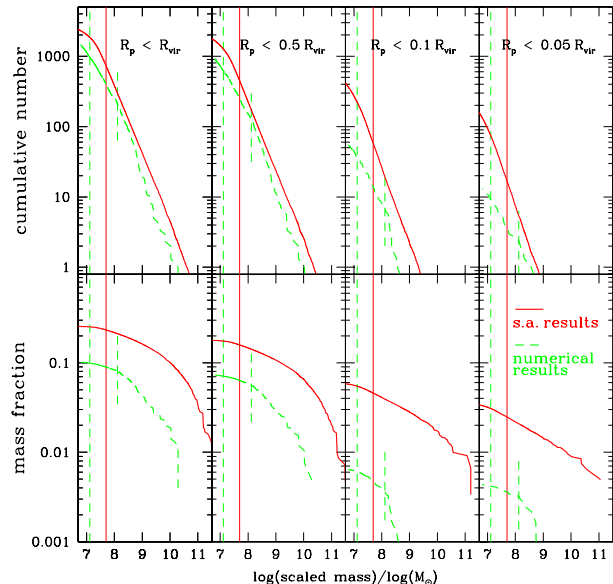


**Figure 11.** (Top panel) Cumulative mass functions for subhaloes within some projected radius  $R_p$ , for model B (solid lines) and Virgo IIa (dashed lines). (Bottom Panel) The fraction of the projected mass within  $R_p$  contained in subhaloes of mass  $M$  or larger. The numerical results are the average over three different projections. Vertical lines indicate the resolution limit of them merger tree (solid) and the 32 and 320-particle mass limits of the simulation.

galaxy haloes. This is well within the region where there is evidence for overmerging in the simulations. We can estimate the importance of overmerging by comparing the substructure in our semi-analytic models with the substructure in the numerical simulations, as a function of projected distance from the centre of the halo. Fig. 11 shows the cumulative mass functions (upper panel) and cumulative mass fraction (lower panel) for subhaloes within some projected radius  $R_p$ , for model B (solid lines) and Virgo IIa (dashed lines). (The numerical results are the average over three orthogonal projections.)

Averaged over a large projected radius, the semi-analytic and numerical results disagree by a factor of  $\sim 2$ . At large masses, some of this offset may be due to the dynamical age of the simulated system, as discussed in paper II (cf. paper II, Fig. 15). At the low-mass end, relaxation or other resolution effects may explain the offset, or it may be due to random, halo-to-halo variation.

More worrying, however, is the offset between the numerical and semi-analytic results at small projected radii. We noted in section 4.3 that in the central regions of the halo the density of subhaloes is almost constant in the simulations, but continues to rise in the semi-analytic model. As a result, the projected mass fraction in substructure within the central 5 percent of virial radius ( $\sim 15$  kpc, or roughly the optical radius for a system like the Milky Way) differs by an order of magnitude between the two methods. This difference may be due to overmerging in the simulations, as discussed in section 4.3 and 4.5, or it could reflect the lim-

itations of the group finder used to analyse the simulation, as discussed in Gill et al. (2004a).

It is premature to draw firm conclusions on the true projected mass fraction from these results, for several reasons. First, the results shown here are for SCDM, since the simulations used for comparison with assumed this cosmology. The slightly reduced amplitude of the cumulative mass function seen in LCDM haloes (see paper II) could affect the projected quantities to some degree. Furthermore, while our dynamical model successfully reproduces the evolution of systems during early stages of mass loss, it may be less accurate for the subhaloes in the centre of the main system, many of which have lost 90 percent of their mass or more (cf. paper II, Fig. 11). Based on Fig. 8, a radical change in the properties of systems stripped to this degree might reduce the central density of subhaloes by a factor of 2, although this would still exceed the density found in the simulations.

Most importantly, however, the semi-analytic model predicts large halo-to-halo scatter, which is correlated with the dynamical state of haloes (cf. paper II, Fig. 15). Thus the comparison between semi-analytic or numerical models and observed systems should account for possible selection effects in the haloes considered. In particular, selecting observed systems on the basis of a particular galaxy morphology (e.g. ellipticals) may correspond to picking haloes that are systematically more relaxed, and thus contain 2–3 times less substructure than average. Finally, neither the semi-analytic nor the numerical results presented here include a galaxy in the potential of the main system, so *both* may overestimate the amount of dark matter substructure in the central regions to some degree.

Despite all these caveats, it is intriguing that our model predicts projected central mass fractions roughly ten times larger than those measured in high-resolution simulations, and that this in turn is close to the value inferred both in early observational estimates (Dalal & Kochanek 2002) and in more recent detailed work (e.g. Metcalf et al. 2004). We will attempt to make more robust estimates of the mass fraction in substructure and discuss the uncertainties in the semi-analytic modelling of central substructure in forthcoming work.

## 5.2 Implications for direct detection

Ultimately, the most convincing way to identify the dark matter particle will be to detect it directly in a terrestrial experiment. There has been a concerted effort for many years to search for the mechanical effects of collisions between dark matter particles and nuclei in calorimeters on Earth (see Pretzl (2002) for a recent review). These experiments have gradually set more and more stringent limits on the dark matter cross-section, without producing a confirmed detection. Tentative evidence for a signal was announced by the DAMA collaboration (cf. Bernabei et al. 2000, 2003), which claimed to see an annual modulation in their event rate, corresponding to the Earth’s changing velocity with respect to the distribution of dark matter in the halo, as it orbits around the Sun. Work of comparable sensitivity by other experiments (e.g. ZEPLIN I – Liubarsky et al. 2000; EDELWEISS – Benoit et al. 2002; CDMS – Akerib et al. 2004) has failed to reproduce this result, however, so it re-

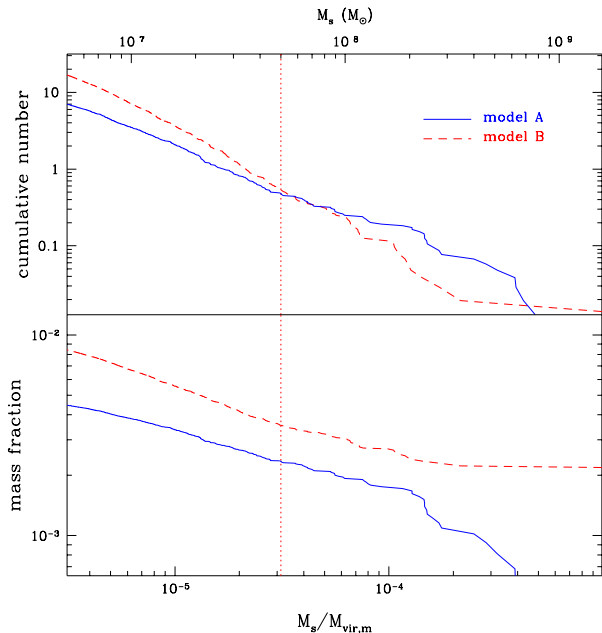


**Figure 12.** Cumulative mass functions and contributions to the total mass within the solar volume (6–10 kpc). The dotted line is for model A, the solid line is for model B.

mains controversial (see Morgan, Green, & Spooner (2004) for a recent summary of the situation).

A crucial factor in interpreting the DAMA result is the regularity of the phase-space distribution of dark matter particles in the solar neighbourhood. Local substructure could introduce additional modulations in the event rate, thereby reducing the sensitivity of experiments looking for an annual signal (Morgan et al. 2004, and references therein). Previous work on the local phase-space distribution of dark matter based on numerical simulations (Helmi et al. 2003) found that substructure was rare in the solar neighbourhood, so that the confusing effects of coherent streams should not be a problem for direct detection experiments. Given the evidence for overmerging in the central regions of simulated haloes presented in section 4.3, however, this conclusion may need to be revised.

We cannot easily compare our semi-analytic predictions with simulated substructure around the position of the Sun, as there is essentially no such substructure in the simulations – the chance of finding a subhalo at around 2 percent of the virial radius is vanishingly small. Instead, we will consider only the uncertainty in the properties of local substructure due to uncertainties in the semi-analytic model. Fig. 12 shows the cumulative mass function of objects in the solar neighbourhood (top panel), and the cumulative contribution to the total mass in that volume. The dotted line is for model A, and the solid line is for model B. We have defined the solar neighbourhood as the region extending from 6 to 10 kpc within our haloes, that is 2–3 percent of the virial radius. The Virgo simulations have no substructure at all within an equivalent volume with respect to the virial radius, and even in the semi-analytic haloes substructure in this region is rare. Nonetheless, we can get a sense of the mass function by averaging over large numbers of trees.

We see that both the mass function and the mass frac-

tion are very sensitive to details of the model. The normalisation of mass fraction in substructure changes by a factor of 1.5–2, but most of this offset comes from the more massive haloes, which are comparatively rare. There is also an appreciable change in the slope of the mass function, however. This is worrying, as direct detection experiments would be sensitive to irregularities on much smaller mass scales than considered here. If we extrapolate assuming model ‘A’, we estimate that roughly 1 percent of mass in the solar neighbourhood would be in substructure of  $10^6 M_\odot$  or more, and that 10 percent would be in substructure of  $10^3 M_\odot$  or more. Extrapolating naively in model ‘B’, on the other hand, most of the mass of the halo could be locked up in fairly massive subhaloes ( $M_s \gtrsim 10^4 M_\odot$ ). These estimates are very unreliable, but they illustrate the fact that on solar mass scales (or spatial scales of roughly a parsec), the distribution of dark matter could be extremely irregular indeed. If local distribution is genuinely this lumpy, then the limits placed by current experiments may be weakened considerably. (Green 2003; Morgan et al. 2004). We will examine the fine structure of local dark matter in detail in future work.

## 6 CONCLUSION

In this paper, we have compared the properties of halo substructure predicted by a semi-analytic model with the substructure identified in a set of self-consistent numerical simulations of halo formation. The semi-analytic model combines merger trees, an algorithm for treating higher-order substructure, and an analytic description of satellite dynamics. While the original treatment of satellite dynamics had several free parameters (TB01), in our full model of halo formation these were fixed by comparison with the high-resolution, restricted simulations of Velazquez and White (1999) and H03, as described in paper I. Thus we have no remaining parametric freedom when comparing the predictions of the semi-analytic model to the numerical results. Our model does make a number of assumptions and approximations, however, concerning the shape and spherical symmetry of the halo density profile, for instance, as well as halo concentrations and subhalo orbits. As discussed in paper II, we estimate that modifying these assumptions would change our results at the 20–30 percent level.

Despite its uncertainties and simplifications, without any adjustment of the parameters the semi-analytic model does an excellent job of matching the numerical results in the outer regions of haloes, where the latter are the most robust. In particular, it matches the overall distribution of subhalo properties and the amplitude of the cumulative distributions of subhalo mass or peak velocity to within 10–20 percent. This is both the level of accuracy expected of our dynamical model, and is also comparable to the intrinsic scatter from one halo to the next, so we conclude that the two methods agree more or less exactly in this regime.

In contrast to this, in the central regions of haloes the semi-analytic model predicts substantially more substructure than is seen in the simulations. The excess subhaloes are predicted to be ancient, dense systems which have orbited in the central part of the halo for most of the age of the universe (10–12 Gyr, or since a redshift of  $z = 2$ ). In the semi-analytic model, these systems survive because the overall

heating and disruption rates are lower than those measured in cosmological simulations. Whether these ancient systems should survive in reality is unclear. The disagreement with semi-analytic and numerical predictions could indicate that our dynamical model for heating and mass loss is systematically less accurate. This seems unlikely, however, since the model is calibrated on the simpler, higher-resolution simulations of Velazquez and White (1999) and H03, and since many of the central subhaloes retain 20–30 percent of their original mass, and thus are at an evolutionary stage where the analytic mass-loss model matches the restricted simulations quite closely.

One physical process recently proposed to explain the higher disruption rate seen in simulations is the increased efficiency of mass loss in systems with anisotropic (internal) velocity distributions (Kazantzidis et al. 2004). Our model is calibrated using simulations of isotropic systems, so in principle anisotropy could affect our results. In the example they consider, however, Kazantzidis et al. find that both fairly strong anisotropy and substantial (80–90 percent) mass loss are required before the evolution of the satellite changes substantially. Further work should clarify the importance of this effect.

The other possibility is that the semi-analytic predictions are essentially correct, and that the simulations analysed in this work are affected by residual overmerging, or by problems with the group finder used to analyse their structure. If overmerging is responsible for the patterns discussed in section 4, higher-resolution numerical work will be required to establish the true level of substructure in the centres of CDM haloes definitively. In particular, based on the arguments of section 4.5, the properties of substructure in current simulations may be unreliable within the central 10 percent of the virial radius (or 30 kpc for a system like the Milky Way), and it may take an increase of  $\sim 100$  or more in mass resolution to get convergent results down to the equivalent of the solar radius. A similar increase in resolution would be required to increase the relaxation time in a subhalo at the nominal resolution limit of current simulations ( $\sim 10^{-5} M_{\text{vir,m}}$ ), and that formed at  $z = 2$ , until it was longer than the Hubble time. Thus while future numerical work can eventually resolve this issue definitively, achieving the required mass and force resolution will remain challenging for some time.

Whatever the final answer to the problem, we have illustrated through several examples that the survival of substructure in the innermost parts of haloes is extremely important to the analysis of many recent observational and experimental results. As it stands, our semi-analytic model provides a robust and computationally efficient basis for studying a wide range of problems related to halo structure and substructure, including the origin and evolution of galaxy morphology, tidal disruption of dwarf galaxies and globular clusters, direct detection of dark matter particles and the local phase-space density of dark matter, indirect detection of dark matter decay products such as gamma-rays and positrons, and the analysis of strong-lensing systems. We will explore these topics in future papers.

**ACKNOWLEDGEMENTS**

The authors wish to thank E. Hayashi, S. Ghigna, B. Moore, J. Navarro and T. Quinn for providing data from their simulations for comparison with our model. We also wish to thank E. Hayashi, T. Kolatt, A. Kravtsov, J. Navarro, J. Silk, and S. White for helpful discussions. JET gratefully acknowledges the support of a postgraduate scholarship from the Natural Sciences & Engineering Research Council of Canada (NSERC) during the initial stages of this work, and support from the Leverhulme Trust and from the UK Particle Physics and Astronomy Research Council (PPARC) in the latter stages. AB gratefully acknowledges support from NSERC through the Discovery and the Collaborative Research Opportunities (CRO) grant programs.

**REFERENCES**

- Akerib, D. S., et al. [The CDMS Collaboration] 2004, *Phys. Rev. Lett.*, submitted (astro-ph/0405033)
- Benoit, A. et al. [The EDELWEISS Collaboration] 2004, *Phys. Rev. Lett. B*, 545 43-49
- Bernabei, R. et al. [The DAMA Collaboration] 2000, *Phys. Rev. Lett. B*, 480, 23
- Bernabei, R. et al. [The DAMA Collaboration] 2003, *Riv. Nuovo Cim.*, 26N1, 1
- Chen, J., Kravtsov, A. V., & Keeton, C. R. 2003, *ApJ*, 592, 24
- Dalai, N. & Kochanek, C. S. 2002, *ApJ*, 572, 25
- De Lucia, G., Kauffmann, G., Springel, V., White, S. D. M., Lanzoni, B., Stoehr, F., Tormen, G., & Yoshida, N. 2004, *MNRAS*, 348, 333
- Desai, V., Dalcanton, J. J., Mayer, L., Reed, D., Quinn, T., & Governato, F. 2004, *MNRAS*, 351, 265
- Diemand, J., Moore, B., Stadel, J., & Kazantzidis, S. 2004, *MNRAS*, 348, 977
- Diemand, J., Moore, B., & Stadel, J. 2004, *MNRAS*, 290
- Diemand, J., Moore, B., & Stadel, J. 2004, *MNRAS*, 352, 535
- D'Onghia, E., Lake, G. 2004, *ApJ*, in press (astro-ph/0309735)
- Eke, V. R., Navarro, J. F., & Steinmetz, M. 2001, *ApJ*, 554, 114 (ENS01)
- Evans, N. W. & Witt, H. J. 2003, *MNRAS*, 345, 1351
- Gao, L., De Lucia, G., White, S. D. M., & Jenkins, A. 2004, *MNRAS*, 352, L1
- Gao, L., White, S. D. M., Jenkins, A., Stoehr, F., & Springel, V. 2004, *MNRAS*, submitted (astro-ph/0404589)
- Gavazzi, R., Mellier, Y., Fort, B., Cuillandre, J.-C., & Dantel-Fort, M. 2004, *AAP*, 422, 407
- Ghigna, S., Moore, B., Governato, F., Lake, G., Quinn, T., & Stadel, J. 1998, *MNRAS*, 300, 146 (G98)
- Ghigna, S., Moore, B., Governato, F., Lake, G., Quinn, T., & Stadel, J. 2000, *ApJ*, 544, 616 (G00)
- Gill, S. P. D., Knebe, A., & Gibson, B. K. 2004a, *MNRAS*, 351, 399
- Gill, S. P. D., Knebe, A., Gibson, B. K., & Dopita, M. A. 2004b, *MNRAS*, 351, 410
- Governato F., Ghigna S., Moore B., 2001, in *ASP Conf. Ser.* 245: *Astrophysical Ages and Times Scales*, 469
- Green, A. M. 2003, *Phys. Rev. D*, 68, 023004
- Hayashi, E., Navarro, J. F., Taylor, J. E., Stadel, J., & Quinn, T. 2003, *ApJ*, 584, 541 (H03)
- Helmi, A., White, S. D. M., & Springel, V. 2003, *MNRAS*, 339, 834
- Inoue, K. T. & Chiba, M. 2003, *ApJL*, 591, L83
- Kauffmann, G., Colberg, J. M., Diaferio, A., & White, S. D. M. 1999, *MNRAS*, 303, 188
- Kazantzidis, S., Mayer, L., Mastrogiuseppe, C., Diemand, J., Stadel, J., & Moore, B. 2004, *ApJ*, 608, 663
- Khochfar, S., & Burkert, A. 2003, *MNRAS*, submitted (astro-ph/0309611)
- Kim, T.-S., Viel, M., Haehnelt, M. G., Carswell, R. F., & Cristiani, S. 2004, *MNRAS*, 347, 355
- Klypin, A., Gottlöber, S., Kravtsov, A. V., & Khokhlov, A. M. 1999, *ApJ*, 516, 530
- Klypin, A., Kravtsov, A. V., Valenzuela, O., & Prada, F. 1999, *ApJ*, 522, 82
- Liubarsky, I., et al. 2000, *Nucl. Phys. B*, (Proc. Suppl.), 87, 64
- Mathis, H., Lemson, G., Springel, V., Kauffmann, G., White, S. D. M., Eldar, A., & Dekel, A. 2002, *MNRAS*, 333, 739
- Metcalfe, R. B. 2004, *apJ*, submitted (astro-ph/0407298)
- Metcalfe, R. B., Moustakas, L. A., Bunker, A. J., & Parry, I. R. 2004, *ApJ*, 607, 43
- Moore, B., Katz, N., & Lake, G. 1996, *ApJ*, 457, 455
- Moore, B., Katz, N., Lake, G., Dressler, A., & Oemler, A. 1996, *Nature*, 379, 613
- Moore, B., Governato, F., Quinn, T., Stadel, J., & Lake, G. 1998, *ApJ*, 499, L5 (M98)
- Moore B., Ghigna S., Governato F., Lake G., Quinn T., Stadel J., & Tozzi P., 1999, *ApJ*, 524, L19 (M99a)
- Moore, B., Quinn, T., Governato, F., Stadel, J., & Lake, G. 1999, *MNRAS*, 310, 1147 (M99b)
- Morgan, B., Green, A. M., & Spooner, N. J. C. 2004, preprint (astro-ph/0408047)
- Moustakas, L. A. & Metcalfe, R. B. 2003, *MNRAS*, 339, 607
- Nagai, D., Kravtsov, A. V. 2004, *ApJ*, submitted (astro-ph/0408273)
- Natarajan, P., Kneib, J., & Smail, I. 2002, *ApJL*, 580, L11
- Okamoto, T. & Habe, A. 1999, *ApJ*, 516, 591
- Pretzl, K. 2002, *Space Science Reviews*, 100, 209
- Reed, D., Gardner, J., Quinn, T., Stadel, J., Fardal, M., Lake, G., & Governato, F. 2003, *MNRAS*, 346, 565
- Reed, D., Governato, F., Quinn, T., Gardner, J., Stadel, J., Lake, G. 2004, *MNRAS*, submitted (astro-ph/0406034)
- Rhodes, J., Refregier, A., Collins, N. R., Gardner, J. P., Groth, E. J., & Hill, R. S. 2004, *ApJ*, 605, 29
- Schechter, P. L. & Wambsganss, J. 2002, *ApJ*, 580, 685
- Spergel, D. N. et al. 2003, *ApJS*, 148, 175
- Springel, V., White, S. D. M., Tormen, G., & Kauffmann, G. 2001, *MNRAS*, 328, 726
- Stadel, J. 2001, Ph.D. thesis, University of Washington
- Stoehr, F., White, S. D. M., Tormen, G., & Springel, V. 2002, *MNRAS*, 335, L84
- Taylor, J. E. 2002, Ph.D. thesis, University of Victoria (<http://wwwlib.umi.com/dissertations/fullcit/NQ62530>)
- Taylor, J. E. & Babul, A. 2001, *ApJ*, 559, 716
- Taylor, J. E. & Babul, A. 2004, *MNRAS*, 348, 811
- Taylor, J. E. & Babul, A. 2004b, *MNRAS*, submitted (paper III)
- Taylor, J. E., & Navarro, J. F. 2001, *ApJ*, 563, 483
- Tegmark, M., et al. 2004, *ApJ*, 606, 702
- van Kampen, E. 1995, *MNRAS*, 273, 295
- Velazquez, H. & White, S. D. M. 1999, *MNRAS*, 304, 254
- Weller, J., Ostriker J. P., & Bode, P. 2004, *MNRAS*, submitted (astro-ph/0405445)
- Yonehara, A., Umemura, M., & Susa, H. 2003, *PASJ*, 55, 1059
- Zentner, A. R. & Bullock, J. S. 2003, *ApJ*, 598, 49



Table I: Numerical Simulations

name	output redshift	virial mass $M_{\text{vir,m}}$ ( $M_{\odot}$ )	virial radius $r_{\text{vir,m}}$ (kpc)	particle mass $m_{\text{p}}$ ( $M_{\odot}$ )	softening $r_{\text{s}}$ (kpc)	number of subhaloes $r < r_{\text{vir,m}}$	$M_{\text{vir,m}}/m_{\text{p}}$ (millions)	$r_{\text{s}}/r_{\text{vir,m}}$ (%)	references
Coma	0.0	$2.37 \times 10^{15}$	3580	$8.6 \times 10^8$	10.0	2302	2.76	0.28	M98
Virgo I	0.0	$4.1 \times 10^{14}$	1995	$8.6 \times 10^8$	10.0	295	0.48	0.5	M98
Virgo IIa	0.0	$4.3 \times 10^{14}$	2026	$1.1 \times 10^8$	1.0	1110	4.00	0.049	G98,G00
Virgo IIb	0.1	$3.98 \times 10^{14}$	1795	$1.1 \times 10^8$	1.0	1052	3.71	0.056	G98,G00
Andromeda	0.2	$2.12 \times 10^{12}$	288	$2 \times 10^6$	1.5	250	1.06	0.52	M99a,M99b
Milky Way	0.2	$1.59 \times 10^{12}$	261	$2 \times 10^6$	1.5	280	0.80	0.57	M99a,M99b